

EG-HumanNeRF: Efficient Generalizable Human NeRF Utilizing Human Prior for Sparse View

Zhaorong Wang Yoshihiro Kanamori Yuki Endo
University of Tsukuba

zhaorong.wang1997@gmail.com, {kanamori, endo}@cs.tsukuba.ac.jp

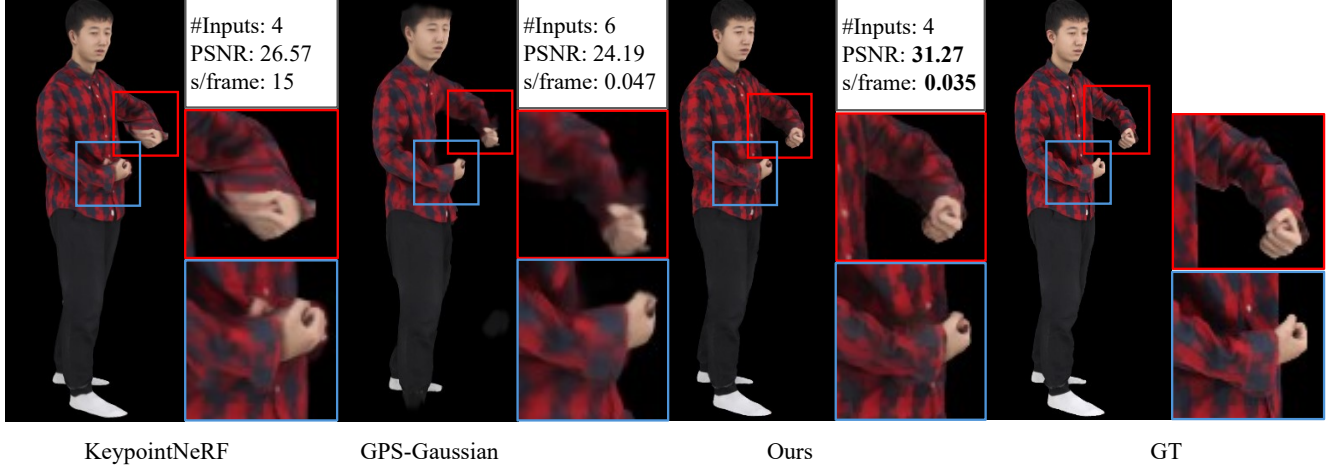


Figure 1. Our method enables efficient and high-quality rendering of generalizable human NeRF from sparse input views. Our method outperforms the state-of-the-art quality-prioritized methods, e.g., KeypointNeRF [29], and has competitive rendering speed with the fastest speed-prioritized methods, e.g., GPS-Gaussian [62]. Our method also removes artifacts caused by occlusion in the input views, often observed in state-of-the-art methods. As shown in the figure, existing methods yield blurriness and missing body parts (red boxes) due to using sparse input views, and finger-like artifacts near the human’s right hand (blue boxes) due to occlusion. In contrast, our method renders high-quality images without artifacts. The metric score and rendering speed in each figure are averaged values over the test set in our experiments.

Abstract

Generalizable neural radiance field (NeRF) enables neural-based digital human rendering without per-scene retraining. When combined with human prior knowledge, high-quality human rendering can be achieved even with sparse input views. However, the inference of these methods is still slow, as a large number of neural network queries on each ray are required to ensure the rendering quality. Moreover, occluded regions often suffer from artifacts, especially when the input views are sparse. To address these issues, we propose a generalizable human NeRF framework that achieves high-quality and real-time rendering with sparse input views by extensively leveraging human prior knowledge. We accelerate the rendering with a two-stage sampling reduction strategy: first constructing boundary meshes

around the human geometry to reduce the number of ray samples for sampling guidance regression, and then volume rendering using fewer guided samples. To improve rendering quality, especially in occluded regions, we propose an occlusion-aware attention mechanism to extract occlusion information from the human priors, followed by an image space refinement network to improve rendering quality. Furthermore, for volume rendering, we adopt a signed ray distance function (SRDF) formulation, which allows us to propose an SRDF loss at every sample position to improve the rendering quality further. Our experiments demonstrate that our method outperforms the state-of-the-art methods in rendering quality and has a competitive rendering speed compared with speed-prioritized novel view synthesis methods.

Table 1. A comparison of the state-of-the-art methods and our method in terms of quality-focused and speed-focused designs. The checkmark (✓) and cross (✗) indicate whether the corresponding item is applicable to each method or not, respectively. Since GPS-Gaussian [62] uses rasterization-based, the ray and sample reduction are not applicable.

	Quality-focused design		Speed-focused design	
Design Method \ Design Method	Human prior	Occlusion awareness	Ray reduction	Sample reduction
IBRNet [50]	✗	✗	✗	✗
KeypointNeRF [29]	✓	✗	✗	✗
GM-NeRF [7]	✓	✗	✗	✓
GP-NeRF [8]	✓	✗	✓	✗
ENeRF [26]	✗	✗	✓	✗
GPS-Gaussian [62]	✗	✗	-	-
Ours	✓	✓	✓	✓

1. Introduction

Digital humans have a wide range of applications, such as telepresence, virtual/augmented reality, and movie production. In recent years, methods based on neural implicit representation (e.g., neural radiance field (NeRF) and its extensions [1, 30, 60]) are utilized for high-quality 3D human rendering. Using human body keypoints and statistical human models such as SMPL [28] and SMPL-X [33] as prior knowledge, the rendering quality is further improved, and the number of input views required is also reduced [34, 54]. Moreover, to overcome the lengthy per-scene retraining of the original NeRF, generalizable human NeRFs [7, 10, 22, 29] utilize pixel-aligned features from input views to enable retraining-free rendering with sparse input views.

However, we find two main issues on rendering speed and quality in the current state-of-the-art generalizable human NeRFs that handle sparse input views. (1) On rendering speed, the inference time of these methods is still slow, as they require dense neural network queries on each ray to render high-quality images. Methods that accelerate the rendering of generalizable human NeRFs have been proposed [8, 26, 62], while they often ignore the human prior knowledge, deteriorating the rendering quality on novel subjects, especially when the input views are sparse. (2) On rendering quality, occluded regions often suffer from artifacts, especially when the input views are sparse, as larger regions are not observable from any input views. While recent work [24, 55] has utilized pretrained generative model as prior knowledge to improve rendering quality for the sparse view setting, they either suffer from rendering speed slowdown by using heavyweight models or do not explicitly handle occluded regions.

To address the above issues, we propose EG-HumanNeRF, aiming at accelerating the rendering of

generalizable human NeRFs while improving the rendering quality, especially in occluded regions under a sparse input view setting. We achieve our goals by further exploiting human prior knowledge than previous methods to reduce neural network queries, provide geometry guidance, and hint for occlusion information. To accelerate the rendering, we propose a two-stage sampling reduction strategy: (1) In the first stage, we construct boundary meshes around the human geometry and perform the first-stage sampling only within the boundary meshes to extract geometry features. (2) In the second stage, from the geometry features, the sampling range is further narrowed down by regressing sampling guidance based on signed ray distances function (SRDF) [63]. SRDF is defined as the signed distance to the nearest surface along a ray, which allows us to regress a narrow sampling range for rendering. The actual neural rendering in the second stage only needs a few samples without rendering quality degradation. To improve the rendering quality in a sparse input setting, especially in occluded regions, we propose an occlusion-aware attention mechanism to hint the network for occlusion region locations. An image space refinement network utilizes the regressed occlusion information to improve rendering quality in occluded regions without introducing heavyweight models. The image space refinement network also performs upsampling, which reduces the number of rays to sample and accelerates the rendering process further. Furthermore, thanks to the SRDF formulation we propose an SRDF loss to supervise the predicted geometry at every sample position when the ground-truth geometry is available, further improving the rendering quality.

The experiments in Sec. 4 demonstrate that our method outperforms the state-of-the-art methods in terms of rendering quality and has competitive rendering speed with the fastest NeRF-based and even 3D

Gaussian-based methods, as illustrated in Fig. 1. A comparison of our method with the state-of-the-art methods on designs for rendering quality and speed is summarized in Table 1. In summary, our main contributions are as follows:

- We propose a generalizable human NeRF framework that utilizes human prior knowledge for both high-quality and efficient rendering using as sparse as three to four input views.
- Utilizing the SMPL-X mesh as human prior knowledge, we reduce the number of ray samples requiring neural network inference in a two-stage manner. Specifically, we reduce the ray samples for both sampling guidance regression and volume rendering, which significantly accelerates the rendering process.
- We predict occluded regions in the target view with human prior knowledge and use image space refinement to improve rendering quality in occluded regions.
- By using an SRDF formulation for rendering, we propose an SRDF loss at every sample position to further improve the rendering quality.

2. Related Work

2.1. Neural Implicit Representation for Human

Traditional 3D construction methods for digital human require dense camera arrays [14, 46, 47] or depth sensors [11, 25, 58] for mesh or volume-based geometry reconstruction. These methods, however, either give unsatisfactory rendering quality because of the limited geometry reconstruction accuracy or require costly hardware setups, hindering their practical use. Neural implicit representation is a promising alternative for representing 3D scenes [30, 37, 41, 49], including full-body human [6, 34, 39, 42, 54] because it enables high-quality rendering without explicit geometry reconstruction. One of the most widely adopted neural implicit representations is neural radiance field (NeRF). NeRF represents the 3D scene as a volumetric radiance field where view-dependent radiances at 3D positions are encoded by multi-layer perceptrons (MLPs). While yielding high-quality rendering results, NeRF requires lengthy neural network training for individual scenes. Follow-up work [4, 50, 57] extends NeRF so that it generalizes on unseen scenes given sparse input views. However, these regression-based methods for general scenes often perform worse than the optimization-based methods unless conducting a post hoc fine-tuning for the specific scene [37, 49]. For humans, prior knowledge of human pose and body shape, such as keypoints and statistical models [28, 33], can be used to guide the view synthesis [7, 10, 22, 29], improving rendering quality on

novel subjects. Nevertheless, the inference time of these methods is still slow, as they require a large number of neural network queries on each ray to render high-quality images. Our method accelerates the rendering of generalizable human NeRFs while utilizing prior knowledge, enabling both efficient and high-quality rendering with sparse inputs.

Existing work [18–20] studied on improving the rendering quality for NeRF when using sparse inputs. A specific issue when using sparse views for novel view synthesis is that regions non-observable from inputs may contain artifacts. Pretrained generative models are often utilized to hallucinate the occluded regions. ReconFusion [55] trains a diffusion model for generalizable novel view synthesis, which is then used to guide the training of an optimization-based NeRF on occluded regions. The heavyweight diffusion model, however, is unsuitable for retraining-free real-time rendering. While ID-NeRF [24] distills a pretrained diffusion model into a generalizable NeRF to improve rendering quality with sparse inputs, the guidance from the diffusion model applies only to the input view features, making its ability to hallucinate occluded regions questionable. To avoid slowing down the rendering process, our method, on the other hand, first extracts occlusion information from human prior knowledge, making the subsequent image space refinement for occluded regions efficient and lightweight.

2.2. Neural Volume Rendering Acceleration

Variant methods have been proposed to accelerate the rendering of NeRF. A few strategies for accelerating both NeRF training and inference include representing the scene with a sparse feature field and shallow MLPs instead of deep MLPs to save computation on each ray sample [3, 5, 27, 31, 43, 56], using image space upsampling to reduce the number of rays to calculate [2, 13, 48], and using efficient sampling strategies to reduce the number of samples [17, 21, 32]. Some methods focus on inference (rendering) acceleration by baking the outputs of the neural network into a sparse feature volume [15, 36] or polygons [9], or extracting boundary meshes to restrict the sampling space as in Adaptive Shells [53]. Our method also utilizes boundary meshes for efficient sampling, but the fine-grained boundary meshes used in Adaptive Shells [53] are not available for our retraining-free setting; Adaptive Shells first optimizes radiance fields for specific scenes, then extracts boundary meshes. Instead, we build boundary mesh from the coarse SMPL-X mesh, and use a second-stage sampling range regression to compensate for the coarse boundary mesh and further reduce the number of samples.

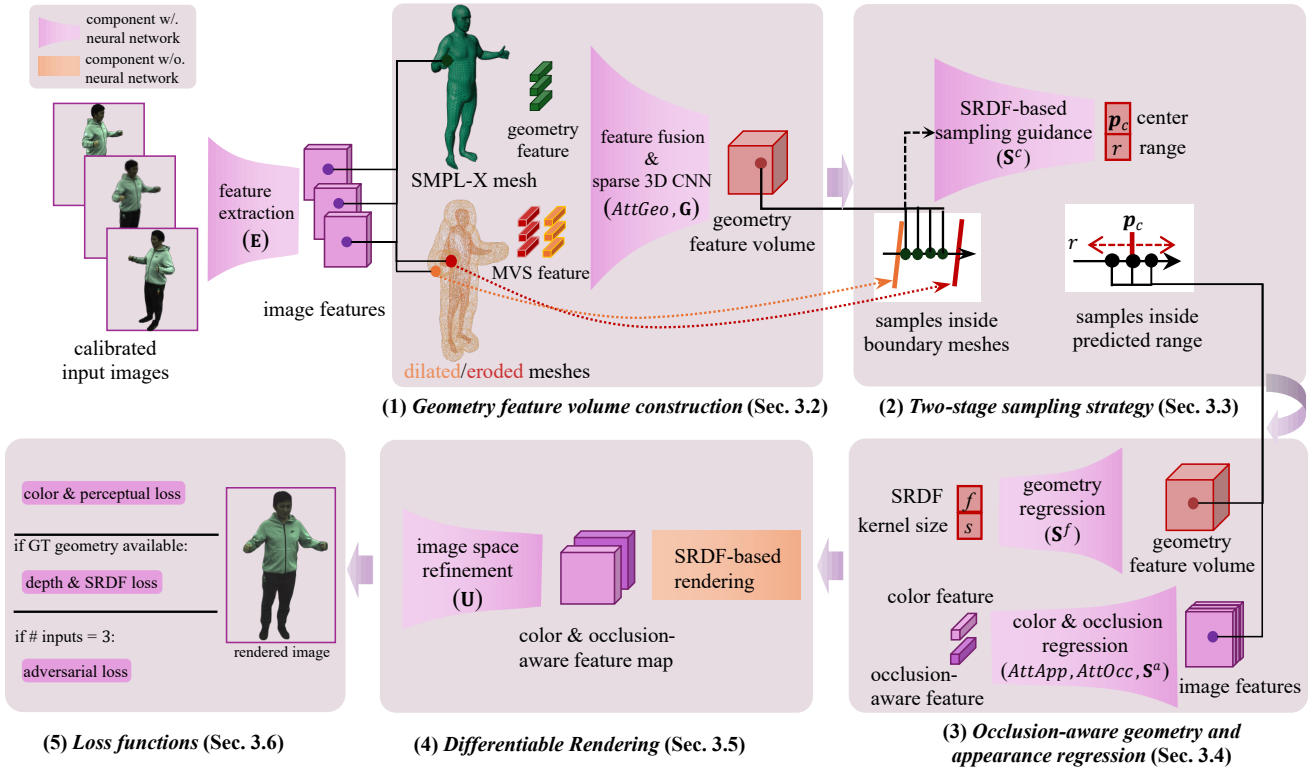


Figure 2. Overview of our method. Given calibrated sparse multi-view images, we encode their feature maps and (1) construct a geometry feature volume from the SMPL-X mesh and the input views to provide human prior knowledge. Utilizing the boundary meshes derived from the SMPL-X mesh, we (2) use a two-stage sampling strategy to reduce the number of samples required and accelerate the rendering while maintaining rendering quality. At each sample position, we (3) regress geometry-related values and appearance features used for rendering, along with an optional occlusion-aware feature to improve rendering quality in occluded regions. We aggregate features on sample positions using an SRDF-based formulation. Finally, we (4) conduct image space refinement from feature maps to synthesize the image in the target view. Our method (5) is trained end-to-end, with optional SRDF and adversarial losses to improve the rendering quality further.

The following works focus on accelerating the rendering of generalizable human NeRF. GP-NeRF [8] and ENeRF [26] achieve efficient rendering by reducing the number of sample positions in volume rendering. GP-NeRF constructs a feature volume from SMPL mesh and utilizes the volume to eliminate samples outside the volume. ENeRF [26] constructs a cost volume to estimate depth that guides the sampling. However, ENeRF does not employ prior knowledge of the human body, deteriorating the rendering quality on novel subjects, especially when the input views are sparse. GPS-Gaussian [62] regresses parameters of 3D Gaussians from the input views to enable fast rendering without neural network inference. However, GPS-Gaussian requires adjacent views to contain fully overlapping subjects for regressing the positions of 3D Gaussians, making it inapplicable to as sparse as three or four input views. Moreover, GPS-Gaussian shares the same limitation as ENeRF in that it does not utilize prior

knowledge of the human body, leading to degradation in rendering quality even with denser input views (e.g., six views in our experiments). A concurrent work conceptually similar to our approach, GHG [23], utilizes human prior for 3D Gaussian by learning the parameters of the 3D Gaussians in the UV space defined by the SMPL-X model. While GHG adopts the fast rendering paradigm of volume splatting, we propose an alternative approach for volume rendering.

3. Method

3.1. Overview

Fig. 2 illustrates our generalizable human NeRF framework. From calibrated sparse multi-view images, our method utilizes the SMPL-X parametric model as both the prior knowledge and the sampling guidance to learn a neural implicit representation that can generalize to novel subjects and render in real time. To render a novel

view, we first construct a geometry feature volume from the SMPL-X mesh and the input views (Sec. 3.2). The feature volume is sparse and contains human geometry prior only around the human surface, enabling an efficient 3D sparse convolution for feature aggregation. We use a two-stage sampling strategy so that it only requires a small number of samples to render high-quality images, accelerating the rendering process (Sec. 3.3). Specifically, from the geometry feature volume, we first take a small number of ray samples within the boundary meshes derived from the SMPL mesh. With the sampled features, we regress signed ray distances as sampling guidance, further reducing the number of second-stage samples required for volume rendering. At each sample position taken in the second stage, we sample the geometry volume, and input view features encoded by a convolutional neural network (CNN) to regress geometry-related values and appearance features used for rendering (Sec. 3.4). When the unobserved regions in the target view are large (i.e., when three input views are used), we regress occlusion-aware features from the SMPL-X mesh and the input views, which are used in later steps to improve rendering quality in occluded regions. Finally, we aggregate features on sample positions using an SRDF formulation followed by a 2D CNN to refine and render the final image (Sec. 3.5). When the occlusion-aware features are available, we predict the occlusion mask to aid the refinement of occluded regions. The 2D CNN also serves as an upsampler to reduce the number of rays to calculate before convolutions, thus further accelerating the rendering process. Our method is trained end-to-end with a color and a perceptual loss. When the ground-truth geometry is available, we also supervise the predicted geometry with an SRDF loss to further improve the rendering quality (Sec. 3.6). When the occlusion-aware refinement is enabled, we use an additional adversarial loss along with a discriminator to fine-tune a trained model, improving the rendering quality in occluded regions.

3.2. Geometry Feature Volume Construction

To provide prior knowledge on human geometry and guidance for efficient sampling, we construct a geometry feature volume by aggregating multi-view image features and human geometry prior from the SMPL-X mesh. Our method starts from N_I calibrated multi-view images $\{I_i \in \mathbb{R}^{H \times W \times 3}\}_{i=1}^{N_I}$ (where H and W are the image height and width) of a human subject and a fitted SMPL-X mesh with vertices $\{\mathbf{v}_j \in \mathbb{R}^3\}_{j=1}^{N_v}$. From the SMPL-X mesh, we construct a pair of dilated and eroded meshes consisting of mesh vertices $\{\mathbf{v}_j^d \in \mathbb{R}^3\}_{j=1}^{N_v}$ and $\{\mathbf{v}_j^e \in \mathbb{R}^3\}_{j=1}^{N_v}$, respectively, by expanding and shrinking the mesh along the normal directions to a fixed

distance. The pair of boundary meshes are used for geometry feature volume construction and sampling guidance. Specifically, for the case of a ray intersecting the both dilated and eroded meshes, we sample uniformly between the first intersections with the dilated and eroded meshes. For the case of a ray intersecting only the dilated mesh, we sample uniformly between the first and last intersections with the dilated mesh. We first extract N_I feature maps $\{I_i^h \in \mathbb{R}^{H^h \times W^h \times C^h}\}_{i=1}^{N_I}$ (where H^h , W^h , and C^h are the height, width, and number of channels of the feature maps, respectively) from the input images using a pretrained CNN \mathbf{E} based on EfficientNet [45]. Given a 3D position $\mathbf{p} \in \mathbb{R}^3$ and the feature map I_i^h , we can project \mathbf{p} to the image plane of an input view via coordinate transformation from the world coordinate to the input camera coordinate $\Pi_i(\cdot)$, followed by a bi-linear interpolation $\Phi_{bi}(\cdot)$. Namely, a pixel-aligned feature $\mathbf{h}_i(\mathbf{p})$ is obtained by

$$\mathbf{h}_i(\mathbf{p}) = \Phi_{bi}(I_i^h, \Pi_i(\mathbf{p})). \quad (1)$$

Substituting \mathbf{p} with the mesh vertex positions \mathbf{v}_j , \mathbf{v}_j^d , and \mathbf{v}_j^e , we obtain the features $\mathbf{h}_i(\mathbf{v}_j)$, $\mathbf{h}_i(\mathbf{v}_j^d)$, and $\mathbf{h}_i(\mathbf{v}_j^e)$ at vertices of SMPL-X, dilated, and eroded meshes, respectively. To provide sufficient information for the neural network to learn the human geometry, we aggregate the multi-view image feature $\{\mathbf{h}_i(\mathbf{v}_j)\}_{i=1}^{N_I}$ along with the human geometry prior, namely, the normal direction \mathbf{n}_j of each SMPL-X vertex using the attention mechanism in GM-NeRF [7] (i.e., Eq. (3) in the paper) as $\mathbf{a}(\mathbf{v}_j) = \text{AttGeo}(\{\mathbf{h}_i(\mathbf{v}_j), \mathbf{d}_i(\mathbf{v}_j)\}_{i=1}^{N_I}, \mathbf{n}_j)$, where $\mathbf{d}_i(\mathbf{v}_j)$ is the direction from the i -th input camera position to the vertex \mathbf{v}_j . Notice that feature $\mathbf{a}(\mathbf{v}_j)$ only provides the geometry information on each SMPL-X vertex, which can be inaccurate. To provide denser information around the human body, we further provide multi-view stereo information around the surface of the human body. Specifically, we aggregate the multi-view image feature $\mathbf{h}_i(\mathbf{v}_j^d)$ and $\mathbf{h}_i(\mathbf{v}_j^e)$ by calculating their mean and variance of input views and concatenating them to produce $\mathbf{m}(\mathbf{v}_j^d)$ and $\mathbf{m}(\mathbf{v}_j^e)$. The features $\{\mathbf{a}(\mathbf{v}_j), \mathbf{m}(\mathbf{v}_j^d), \mathbf{m}(\mathbf{v}_j^e)\}_{j=1}^{N_v}$ are then fed into a sparse 3D convolutional network \mathbf{G} to construct the geometry feature volume $\mathcal{G} \in \mathbb{R}^{D_\mathcal{G} \times H_\mathcal{G} \times W_\mathcal{G} \times C_\mathcal{G}}$, where $D_\mathcal{G}$, $H_\mathcal{G}$, $W_\mathcal{G}$, and $C_\mathcal{G}$ are the depth, height, width, and the number of channels of the feature volume, respectively.

3.3. Two-stage Sampling Strategy

We propose a two-stage sampling strategy to reduce the total number of samples that require neural network inference, accelerating the rendering process while maintaining rendering quality. In the first stage, we sample the geometry feature volume on each ray to regress the sampling guidance for the second stage. Instead

of sampling inside the scene bounding box, we utilize the dilated and eroded boundary meshes constructed to sample within, skipping the empty space. Formally, given a ray \mathbf{r} and the geometry feature volume \mathcal{G} , we first uniformly sample a set of 3D positions $\{\mathbf{p}_k\}_{k=1}^K$ inside the boundary meshes and extract the corresponding geometry feature $\mathbf{g}(\mathbf{p}_k) = \Phi_{tri}(\mathcal{G}, \mathbf{p}_k)$, where $\Phi_{tri}(\cdot)$ is the tri-linear interpolation operator. In the second stage, to further reduce the number of samples required for rendering, we specify the sampling range by regressing a sampling center \mathbf{p}_c and sampling radius r , for each ray using an SRDF formulation. From the geometry features \mathbf{g}_k and the ray direction \mathbf{d} , we regress the signed ray distances $\{f_k\}_{k=1}^K$ along with a confidence score $\{c_k\}_{k=1}^K$ using a shallow MLP \mathbf{S}^c :

$$(f_k, c_k) = S^c(\mathbf{g}_k, \mathbf{d}). \quad (2)$$

The sampling center \mathbf{p}_c is then calculated as a weighted average of the 3D positions calculated from the SRDFs:

$$\mathbf{p}_c = \frac{1}{\sum_{k=1}^K c_k} \sum_{k=1}^K c_k (\mathbf{p}_o + f_k \mathbf{d}), \quad (3)$$

where \mathbf{p}_o is the camera position of the target view. The sampling radius r is calculated as the standard deviation of weighted distances between the 3D positions and \mathbf{p}_c :

$$r = \left(\frac{1}{\sum_{k=1}^K c_k} \sum_{k=1}^K c_k (\mathbf{p}_o + f_k \mathbf{d} - \mathbf{p}_c)^2 \right)^{\frac{1}{2}}. \quad (4)$$

The advantage of predicting SRDFs instead of the ray parameter directly is that we can use an SRDF loss (Sec. 3.6) to supervise the SRDFs at every sample position, which helps further improve the rendering quality when the ground-truth geometry is available. We uniformly sample L 3D positions $\{\mathbf{p}_l = \mathbf{p}_c + t_l \mathbf{d}\}_{l=1}^L$, where $t_l \in [-r, r]$. Namely, we sample 3D positions within radius r from center \mathbf{p}_c to render the novel view.

With the strong geometry guidance provided by the boundary meshes and the geometry feature volume, it only requires a small number of L samples to render high-quality images.

3.4. Occlusion-aware Geometry and Appearance Regression

Given the guided sample positions, we regress geometry and appearance values or features at sample positions for rendering, which we describe in Sec. 3.4.1.

Different from previous work, we optionally use an attention mechanism to regress an occlusion-aware feature (Sec. 3.4.2) from the SMPL-X geometry and the input views when the unobserved regions in the target

view are large. The occlusion-aware features contain information on whether the input views are reliable for the sample position, which is used to regress an occlusion mask, aiding the image space refinement on occluded regions (Sec. 3.5.2).

3.4.1 Geometry and Appearance Regression

Given sample positions $\{\mathbf{p}_l\}_{l=1}^L$, we sample the geometry feature volume \mathcal{G} and the image feature maps $\{I_i^h\}_{i=1}^{N_I}$ at the sample positions to obtain geometry features $\mathbf{g}(\mathbf{p}_l) = \Phi_{tri}(\mathcal{G}, \mathbf{p}_l)$ and image features $\{\mathbf{h}_i(\mathbf{p}_l)\}_{i=1}^{N_I}$, with $\mathbf{h}_i(\mathbf{p}_l) = \Phi_{bi}(I_i^h, \Pi_i(\mathbf{p}_l))$. From the sampled features, geometry-related values, and appearance features, along with colors and occlusion-aware features, are regressed.

Similar to Eq. (2), we use another shallow MLP \mathbf{S}^f to regress the geometry-related values $(f_l, s_l) = S^f(\mathbf{g}(\mathbf{p}_l), \mathbf{d})$. The outputs include an SRDF value f_l and an additional kernel size s_l , which will be used for the rendering process described in Sec. 3.5.

To blend the image features from the input views while considering the geometry, we utilize the attention mechanism in GM-NeRF [7] (i.e., Eq. (5) in the paper) to obtain the appearance features $\mathbf{a}(\mathbf{p}_l) = \text{AttApp}(\{\mathbf{h}_i(\mathbf{p}_l), \mathbf{r}_i(\mathbf{p}_l), \mathbf{d}_i(\mathbf{p}_l)\}_{i=1}^{N_I}, \mathbf{g}(\mathbf{p}_l), \mathbf{d}(\mathbf{p}_l))$, where \mathbf{r}_i , \mathbf{d}_i , and \mathbf{d} are the projected input views raw pixels from \mathbf{p}_l , the input camera ray direction, and the target camera ray direction at \mathbf{p}_l , respectively. We subsequently use another shallow MLP \mathbf{S}^a to regress the RGB color \mathbf{c}_l from the appearance feature $\mathbf{a}(\mathbf{p}_l)$.

3.4.2 Occlusion-aware Attention

In order to improve the rendering quality in occluded regions with a limited model capacity, it is crucial to provide guidance on the exact occlusion regions so that the network can know for which pixels the input view information may not be reliable and should be hallucinated instead of copied from input views. To this end, we propose an occlusion-aware attention mechanism that calculates features indicating whether occlusions exist in input views given a sample position \mathbf{p} . We first render a world-space position map X' of the SMPL-X mesh from the target view and position maps $\{X_i\}_{i=1}^{N_I}$ of the SMPL-X mesh from the input views. We then calculate the distance d_i between \mathbf{p} 's observed positions in the target view and in the i -th input view as follows:

$$\begin{aligned} \mathbf{x}'(\mathbf{p}) &= \Phi_{bi}(X', \Pi'(\mathbf{p})), \\ \mathbf{x}_i(\mathbf{p}) &= \Phi_{bi}(X_i, \Pi_i(\mathbf{p})), \\ d_i(\mathbf{p}) &= \|\mathbf{x}'(\mathbf{p}) - \mathbf{x}_i(\mathbf{p})\|_2. \end{aligned} \quad (5)$$

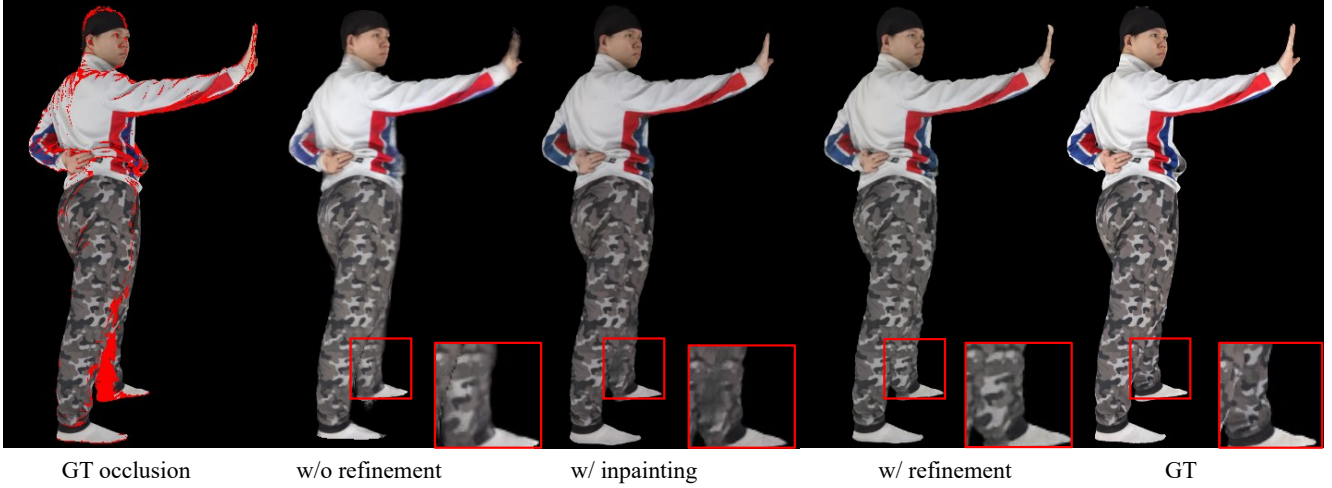


Figure 3. Comparisons between inpainting and image space refinement. “w/o refinement” denotes the rendering results without using image space refinement. “w/ inpainting” denotes rendering results with a post hoc inpainting method [44]. “w/ refinement” denotes our rendering results with image space refinement using occlusion-aware features. When the input views already provide sufficient information to hallucinate the occluded regions, the inpainting method destroys the original information and is not able to recover complex textures without using a heavyweight model. In contrast, the image space refinement method focus on the occluded regions, preserving the original information and avoiding the need for heavyweight generative models.

The distance d_i should be (close to) zero when the target and the i -th input view observe the same position and large when they observe different positions, indicating occlusions. Our occlusion-aware attention that calculates the occlusion-aware feature $\mathbf{o}(\mathbf{p}) = \text{AttOcc}(\{\mathbf{g}(\mathbf{p}), \mathbf{d}(\mathbf{p}), \{d_i(\mathbf{p})\}_{i=1}^{N_I}, \mathbf{x}'(\mathbf{p}), \{\mathbf{x}_i(\mathbf{p})\}_{i=1}^{N_I}\})$ is then formulated as follows:

$$\begin{aligned} \mathbf{Q}_o(\mathbf{p}) &= F_o^Q(\mathbf{g}(\mathbf{p}) \oplus \mathbf{d}(\mathbf{p}) \oplus \mathbf{x}'(\mathbf{p})), \\ \mathbf{K}_o(\mathbf{p}) &= F_o^K\left(\{\mathbf{h}_i(\mathbf{p}) \oplus \mathbf{d}_i(\mathbf{p}) \oplus \mathbf{x}_i(\mathbf{p}) \oplus d_i(\mathbf{p})\}_{i=1}^{N_I}\right), \\ \mathbf{V}_o(\mathbf{p}) &= F_o^V\left(\{\mathbf{g}(\mathbf{p}) \oplus d_i(\mathbf{p})\}_{i=1}^{N_I}\right), \\ \mathbf{o}(\mathbf{p}) &= F_o(\text{Att}(\mathbf{Q}_o(\mathbf{p}), \mathbf{K}_o(\mathbf{p}), \mathbf{V}_o(\mathbf{p}))), \end{aligned} \quad (6)$$

where \oplus denotes the concatenation operation, F_o^Q , F_o^K , and F_o^V are linear layers that produce the query, key, value, and output features, respectively. The intuition behind Eq. (6) is that, while whether \mathbf{p} is occluded or not can be estimated simply from $\min\{d_i\}_{i=1}^{N_I}$, the SMPL-X mesh differs from the ground-truth human geometry, causing inaccuracies in the occlusion estimation. The attention mechanism, however, learns to decide whether the SMPL-X geometry is reliable or not for the occlusion estimation from the geometry feature \mathbf{g} , image feature \mathbf{h}_i , and the input and target view direction \mathbf{d}_i and \mathbf{d} . This attention mechanism is proven to be effective for robustly blending multi-view features in GM-NeRF [7] when the SMPL-X geometry is inaccurate; thus, we adapt this mechanism to handle

occlusion-aware features. We optionally calculate the occlusion-aware features, which will be used in the image space refinement (Sec. 3.5.2) when the unobserved regions in the target view are large, i.e., when three input views are used in our experiment.

3.5. Differentiable Rendering

To render the novel-view image, we first render a low-resolution feature map using the SRDF-based volume rendering method in VolRecon [37]. The feature map is fed into a 2D CNN to predict the final full-resolution image. The purpose of the 2D CNN is two-fold: (1) to reduce calculations that depend on the sample number by reducing the number of rays to sample, and (2) to refine regions fully occluded in input views.

3.5.1 Volumetric Rendering

Given a feature vector \mathbf{f}_l (or a scalar value) at the sample position \mathbf{p}_l , we aggregate the features as follows:

$$\hat{\mathbf{f}} = \sum_{l=1}^L T_l \alpha_l \mathbf{f}_l, \quad (7)$$

where $T_l = \prod_{n=1}^{l-1} (1 - \alpha_n)$ is the transmittance and α_l is the opacity defined as $\alpha_l = 1 - \exp\left(-\int_{t_l}^{t_{l+1}} \sigma(t) dt\right)$, with t_l being the distance from the camera to the l 's sample position. To obtain opaque density $\sigma(t)$ from

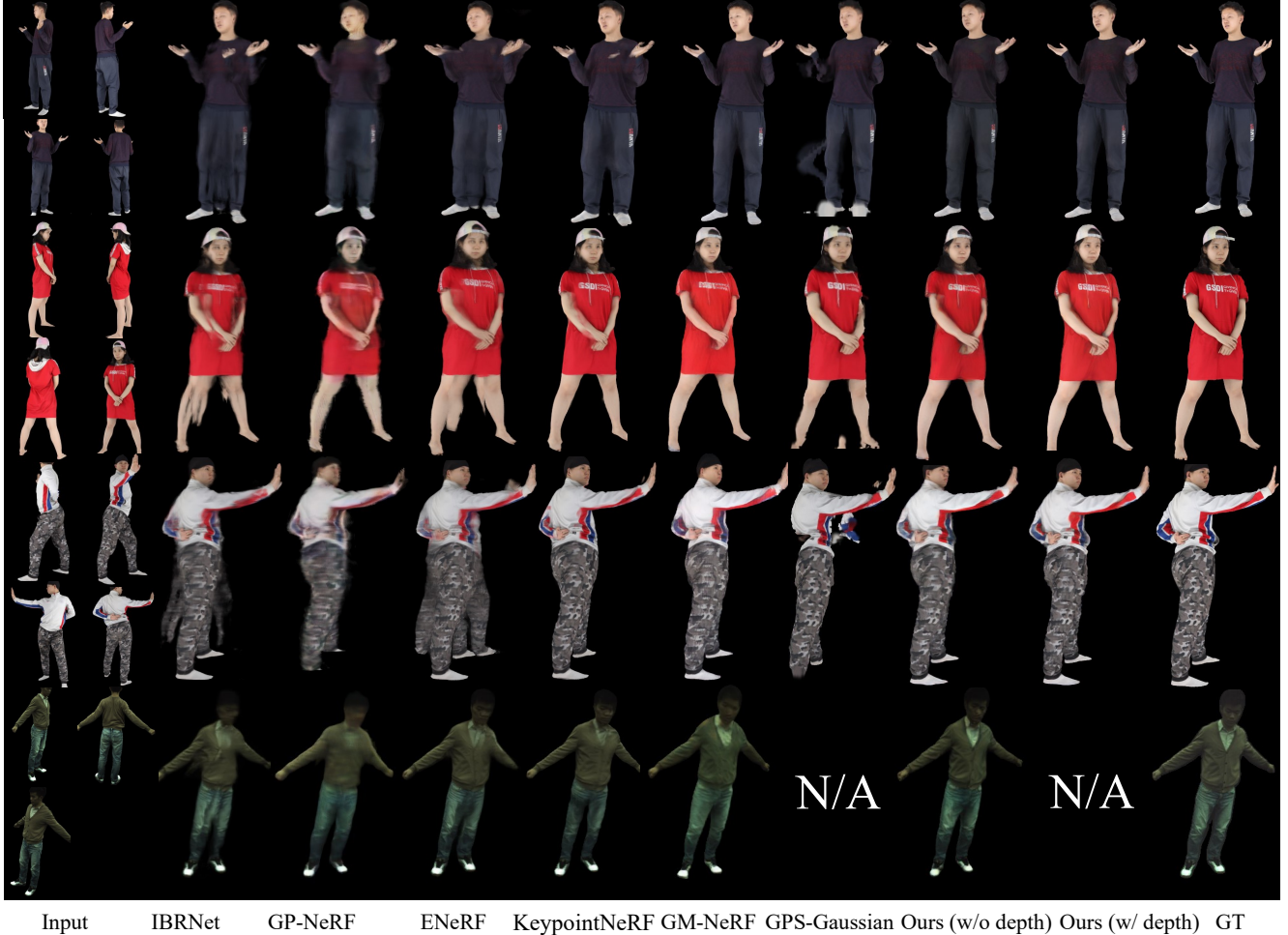


Figure 4. Qualitative evaluation results on the THuman2.0 dataset (first three rows) and the ZJU-MoCap dataset (last row) compared with the state-of-the-art methods. We use four input views for the THuman2.0 dataset and three input views for the ZJU-MoCap dataset. For GPS-Gaussian [62], we use six input views and ground-truth depth instead of four, as six is the minimum number supported by this method.

SRDF f , we adopt the formulation from NeuS [49] and replace the signed distance function with SRDF as done in VolRecon [37] as follows:

$$\sigma(t) = \max \left(-\frac{\frac{d\Phi_s}{dt}(f)}{\Phi_s(f)}, 0 \right), \quad (8)$$

$$\Phi_s(f) = (1 + \exp(-f/s))^{-1},$$

where s is the learnable kernel size controlling the sharpness of the density function. Please refer to VolRecon [37] and NeuS [49] for more theoretical details. We trace the rays at pixels for an image with half of the target resolution and render the low-resolution feature map $\hat{I}_a \in \mathbb{R}^{\frac{H'}{2} \times \frac{W'}{2} \times C_a}$ and $\hat{I}_o \in \mathbb{R}^{\frac{H'}{2} \times \frac{W'}{2} \times C_o}$ for the appearance and occlusion-aware features by substituting \mathbf{f}_l with \mathbf{a}_l and \mathbf{o}_l in Eq. (7), respectively. H' and

W' are the height and width of the target image, respectively. We also calculate a low-resolution RGB and depth image $\hat{I}_{low} \in \mathbb{R}^{\frac{H'}{2} \times \frac{W'}{2} \times 3}$ and $\hat{I}_d \in \mathbb{R}^{\frac{H'}{2} \times \frac{W'}{2}}$ by substituting \mathbf{f}_l with \mathbf{c}_l and t_l .

3.5.2 Occlusion-aware Image Space Rendering

We use a 2D CNN \mathbf{U} to predict the final full-resolution image $\hat{I} \in \mathbb{R}^{H \times W \times 3}$ from the low-resolution feature maps \hat{I}_a , \hat{I}_o , and the RGB image \hat{I}_{low} . Specifically, we first use a shallow 2D CNN \mathbf{O} to predict the occlusion mask $\hat{O} \in \mathbb{R}^{H \times W}$ from the low-resolution occlusion-aware feature map \hat{I}_o . The full-resolution image is cal-

Table 2. Quantitative comparison with state-of-the-art methods on ZJU-MoCap and THuman2.0 datasets. The inference time is measured on a single NVIDIA A6000 GPU, except for IBRNet [50]. * We measured the inference time of IBRNet [50] on an old GPU, NVIDIA Quadro RTX 8000 GPU, because of the old runtime setting of IBRNet’s official implementation.

Method	ZJU-MoCap			THuman2.0			ms/frame
	PSNR \uparrow	SSIM \uparrow	LPIPS \downarrow	PSNR \uparrow	SSIM \uparrow	LPIPS \downarrow	
IBRNet [50]	25.82	0.846	0.178	27.77	0.928	0.098	7374.83*
KeypointNeRF [29]	25.54	0.874	0.104	26.57	0.939	0.055	15097.23
GM-NeRF [7]	26.38	0.881	0.105	28.12	0.944	0.068	253.66
GP-NeRF [8]	24.94	0.863	0.137	26.78	0.918	0.111	158.63
ENeRF [26]	24.54	0.857	0.134	25.66	0.898	0.100	40.33
GPS-Gaussian [62]	N/A	N/A	N/A	24.19	0.921	0.077	46.97
Ours (w/o depth)	26.85	0.891	0.086	<u>29.44</u>	<u>0.951</u>	<u>0.060</u>	34.95
Ours (w/ depth)	N/A	N/A	N/A	31.73	0.973	0.034	34.95

culated as follows:

$$\hat{I} = \mathbf{U}(\hat{I}_a \oplus \hat{I}_o \oplus \text{Downsample}(\hat{O}, \frac{1}{2})) + \text{Upsample}(\hat{I}_{low}, 2), \quad (9)$$

where $\text{Downsample}(\cdot, \frac{1}{2})$ and $\text{Upsample}(\cdot, 2)$ are the bilinear downsampling and upsampling operators, respectively. The CNN \mathbf{U} not only upsamples and decodes the feature map but also improves the rendering quality, especially on occluded regions using the occlusion mask \hat{O} as guidance. With the predicted occlusion mask, an alternative approach to improve the rendering quality in occluded regions would be to mask out the occluded regions on the rendered image and inpaint. However, we observe that such inpainting introduces two issues. Firstly, the occluded regions do not necessarily contain artifacts. Fig. 3 shows that, while part of the patterns (highlighted in “GT occlusion”) on the pants are not observable from the input views, the input views provide similar patterns that can be used to hallucinate the occluded regions even without using image space refinement (shown in “w/o refinement”). Masking out the occluded regions in the case described above destroys available information for hallucination. Secondly, it can be challenging for the inpainting network to generate complex patterns (shown in “w/ inpainting”) unless using a large model capacity, which would slow down the rendering process. Therefore, we argue that the refinement-based method is more flexible in keeping the available information (shown in “w/ refinement”) and hallucinating only when necessary, suiting our task that requires efficient rendering.

3.6. Loss Functions

We train our network in an end-to-end manner using a loss function that includes a color loss \mathcal{L}_{color} and a

perceptual loss \mathcal{L}_{percep} . When using ground-truth depth, we also include a depth loss \mathcal{L}_{depth} , and an SRDF loss \mathcal{L}_{SRDF} . The total loss when using the ground-truth depth is defined as follows:

$$\mathcal{L} = \lambda_{color} \mathcal{L}_{color} + \lambda_{percep} \mathcal{L}_{percep} + \lambda_{depth} \mathcal{L}_{depth} + \lambda_{SRDF} \mathcal{L}_{SRDF}, \quad (10)$$

where λ_* are weights of the corresponding loss functions. The color loss is defined as the ℓ_1 loss between the predicted colors and the ground-truth colors on pixels. The perceptual loss is defined as the ℓ_1 loss between the VGG [40] features of the predicted and the ground-truth images. Both the color and perceptual loss are commonly used in NeRFs for humans [7, 29]. When the input views are as sparse as three, we fine-tune the model trained with \mathcal{L} with loss $\mathcal{L} + \lambda_{adv} \mathcal{L}_{adv}$ additionally using a discriminator \mathbf{D} . \mathcal{L}_{adv} includes a non-saturating adversarial loss, a gradient penalty [38], and a feature matching loss [51], as done in LaMa [44]. We stop the gradient backpropagation for the non-occluded regions in the adversarial loss to avoid hallucination in observable regions.

While our method can generalize to novel subjects without training with ground-truth depth (by setting $\lambda_{depth} = 0$ and $\lambda_{SRDF} = 0$), we can further improve the rendering quality and geometry accuracy when the ground-truth depth is available. We use the depth loss \mathcal{L}_{depth} as the ℓ_1 -distance between the predicted depth map \hat{I}_d and the ground-truth depth map. Thanks to the SRDF-based rendering, we can easily calculate the ground-truth SRDF values for each sample position from the ground-truth depth map and employ the SRDF loss \mathcal{L}_{SRDF} to enforce the SRDFs representing actual surfaces. The SRDF loss \mathcal{L}_{SRDF} is defined as the ℓ_1 -distance between the predicted SRDF values f and the ground-truth SRDF values f^{gt} at the two sets of

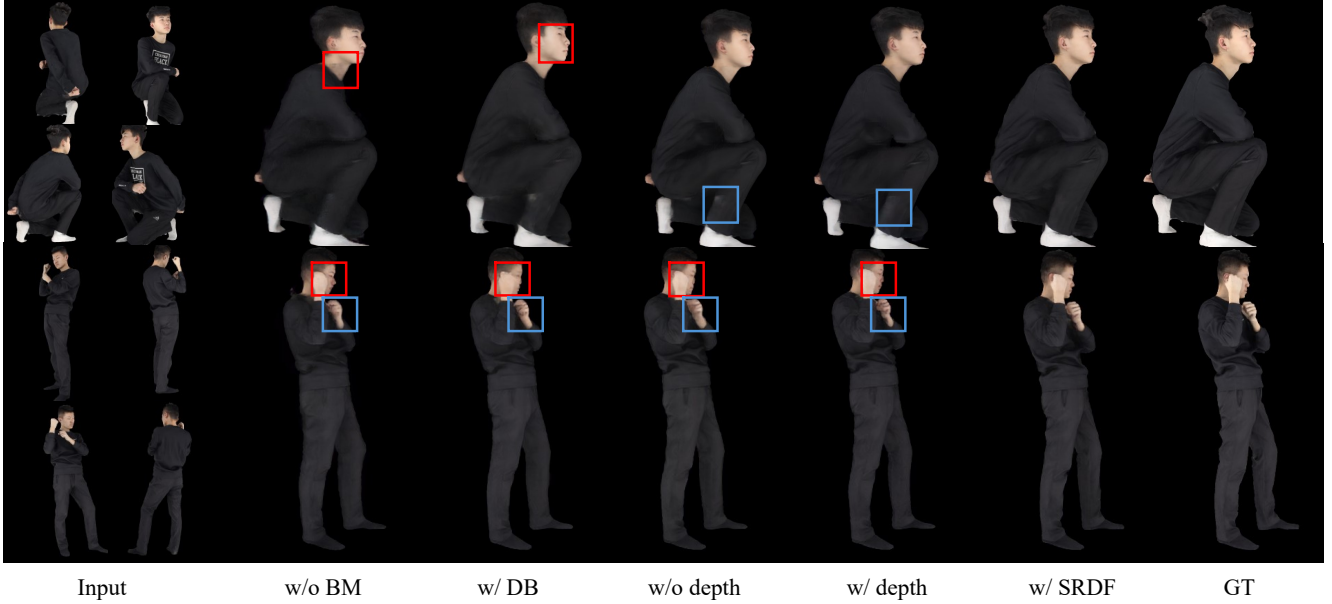


Figure 5. Qualitative results of the ablation studies. “w/o BM” denotes the results without using the boundary meshes. “w/ DB” denotes the results with the density-based rendering. “w/o depth” denotes the results without using the depth loss. “w/ depth” denotes the results with the depth loss only. “w/ SRDF” denotes the results with the depth loss and the SRDF loss. As shown in the red boxes in the first row, results from the model missing components exhibit artifacts on neck or unnatural face. The results from the model without the SRDF loss exhibit slight artifacts on the pants, as shown in the blue boxes in the first row. In the second row, models except for the one using SRDF loss exhibit different extents of artifacts on face and one hand.

ray sampling positions $\{t_k\}_{k=1}^K$ and $\{t_l\}_{l=1}^L$ used for sampling guidance and rendering, respectively. Formally, the SRDF loss is defined as follows:

$$\mathcal{L}_{SRDF} = \frac{1}{K} \sum_{k=1}^K |f(t_k) - f^{gt}(t_k)| + \frac{1}{L} \sum_{l=1}^L |f(t_l) - f^{gt}(t_l)|. \quad (11)$$

To calculate the ground-truth SRDF values $f^{gt}(t)$ at t , we first calculate the ray parameters $\{t_m\}_{m=1}^M$ of intersection points between the ray and the ground-truth human scan with PyTorch3D [35], and then calculate $f^{gt}(t)$ as follows:

$$t_{closest} = \arg \min_{m=1}^M |t - t_m|, \quad (12)$$

$$f^{gt}(t) = t_{closest} - t,$$

where $t_{closest}$ is the ray parameter of the closest intersection point to the sample at t . We observe that the SRDF loss helps to further improve the rendering quality, which will be shown in Sec. 4.3.

4. Experiments

In this section, we show the evaluation of our method for novel view synthesis. We first introduce our ex-

perimental settings, including datasets and implementation details in Sec. 4.1. We compared our method with the state-of-the-art methods on the novel view synthesis task, with results shown in Sec. 4.2. We also conducted ablation studies to analyze the effectiveness of our method, which is shown in Sec. 4.3.

4.1. Experimental Settings

We evaluated our method on two datasets: ZJU-MoCap [34] and THuman2.0 [59]. We introduce the datasets and the evaluation protocol in Sec. 4.1.1 and provide the implementation details in Sec. 4.1.2.

4.1.1 Datasets and Evaluation Protocols

ZJU-MoCap [34] is a real-world multi-view human dataset that contains ten subjects performing various actions. Following the evaluation protocol adopted in KeyPointNeRF [29] and GM-NeRF [7], we split the dataset into seven subjects for training and three subjects for testing using three input views. THuman2.0 [59] is a synthetic human dataset that contains 525 human scan meshes. To render the multi-view images for training, we placed the camera at a distance so that the human height fits the image height and sample a roll

angle uniformly within $[0^\circ, 360^\circ]$ with an interval of 10° . We split the dataset into 400 meshes for training and 125 meshes for testing using four input views with an interval of 90° , aligning with the input view number in GM-NeRF [7]. The angle between target and input views is 45° . The resolution of the input images is 1024×1024 , and the resolution of the rendered images is 512×512 . For evaluation metrics, we adopted peak signal-to-noise ratio (PSNR), structural similarity index (SSIM) [52], and learned perceptual image patch similarity (LPIPS) [61], which are commonly used in the novel view synthesis task. We used a single NVIDIA RTX A6000 GPU for rendering speed evaluation.

Table 3. Ablation studies on the THuman2.0 dataset using four input views. Either removing the boundary meshes or using the density-based rendering reduces the rendering quality. Using the depth loss and the SRDF loss further improves the rendering quality.

Method	PSNR \uparrow	SSIM \uparrow	LPIPS \downarrow
Ours (w/o boundary meshes)	29.08	0.950	0.068
Ours (w/ density-based)	28.69	0.934	0.075
Ours (w/o depth)	29.44	0.951	0.060
Ours (w/ depth only)	29.60	0.968	0.051
Ours (w/ depth & SRDF)	31.73	0.973	0.034

Table 4. Ablation studies on the THuman2.0 dataset to analyze the effectiveness of handling occluded regions. We use three input views to obtain the results. “Ours w/o refinement” denotes the results without using image space refinement. “Ours w/ occlusion-awareness” denotes the results with image space refinement using occlusion-aware features.

Method	PSNR \uparrow	SSIM \uparrow	LPIPS \downarrow
Ours w/o refinement	30.57	0.965	0.048
Ours w/ occlusion-awareness	31.03	0.970	0.035

4.1.2 Implementation Details

We implemented our method using PyTorch. We used Adam optimizer with a learning rate of 10^{-4} and a batch size of one image to train the network until convergence. We set the numbers of samples per ray $K = 16$ for sampling guidance and $K = 8$ for volume rendering. We set the resolution of the geometry feature volume to $224 \times 224 \times 224$. For the loss weights, we set $\lambda_{color} = 150$, $\lambda_{percep} = 0.5$, $\lambda_{adv} = 5$, $\lambda_{depth} = 1$, and $\lambda_{SRDF} = 1$. Please refer to Appendix B for more implementation details.

4.2. Comparisons on Novel View Synthesis

We compared our method with the state-of-the-art generalizable methods that prioritize rendering quality on novel subjects, including IBRNet [50], Keypoint-NeRF [29], and GM-NeRF [7]. We also compared with the speed-prioritized NeRF-based methods, including GP-NeRF [8], ENeRF [26]. We retrained and evaluated the networks of the compared methods on ZJU-MoCap [34] and THuman2.0 dataset [59] using the dataset split and evaluation protocol introduced in Sec. 4.1.1. We implemented GM-NeRF following the description in the paper. For other methods, we used the official implementation and training protocols. Table 2 shows the quantitative comparison results. We observe that our method outperforms the state-of-the-art methods in terms of rendering quality when the ground-truth depths are not available. When using the ground-truth depth, rendering quality of our method is further improved. Fig. 4 shows the qualitative results of our method compared with the state-of-the-art methods. We observe that our method can synthesize high-quality novel views with much less artifacts, blurriness, and better details compared to the state-of-the-art methods. Please refer to Appendix A for more qualitative results. We also compared with the state-of-the-art 3D-Gaussian-based method for human, GPS-Gaussian [62]. GPS-Gaussian requires at least six inputs and the ground-truth depth to synthesize complete human bodies due to its usage of stereo-based depth estimation. We used six input views and ground-truth depth for GPS-Gaussian to obtain the results shown in Table 2. Our method still outperforms GPS-Gaussian even with much fewer input views and without ground-truth depth.

Table 5. Ablation studies of the number of samples per ray on the THuman2.0 dataset. “4 & 2” denotes the number of samples per ray for sampling guidance and rendering, respectively.

Samples	PSNR \uparrow	SSIM \uparrow	LPIPS \downarrow
4 & 2	31.47	0.971	0.036
8 & 4	31.50	0.971	0.035
16 & 8	31.73	0.973	0.034

4.3. Ablation Studies

We conducted ablation studies on the components of our method to analyze their effectiveness (Sec. 4.3.1) and the experimental settings to analyze their impact on the rendering quality (Sec. 4.3.2).

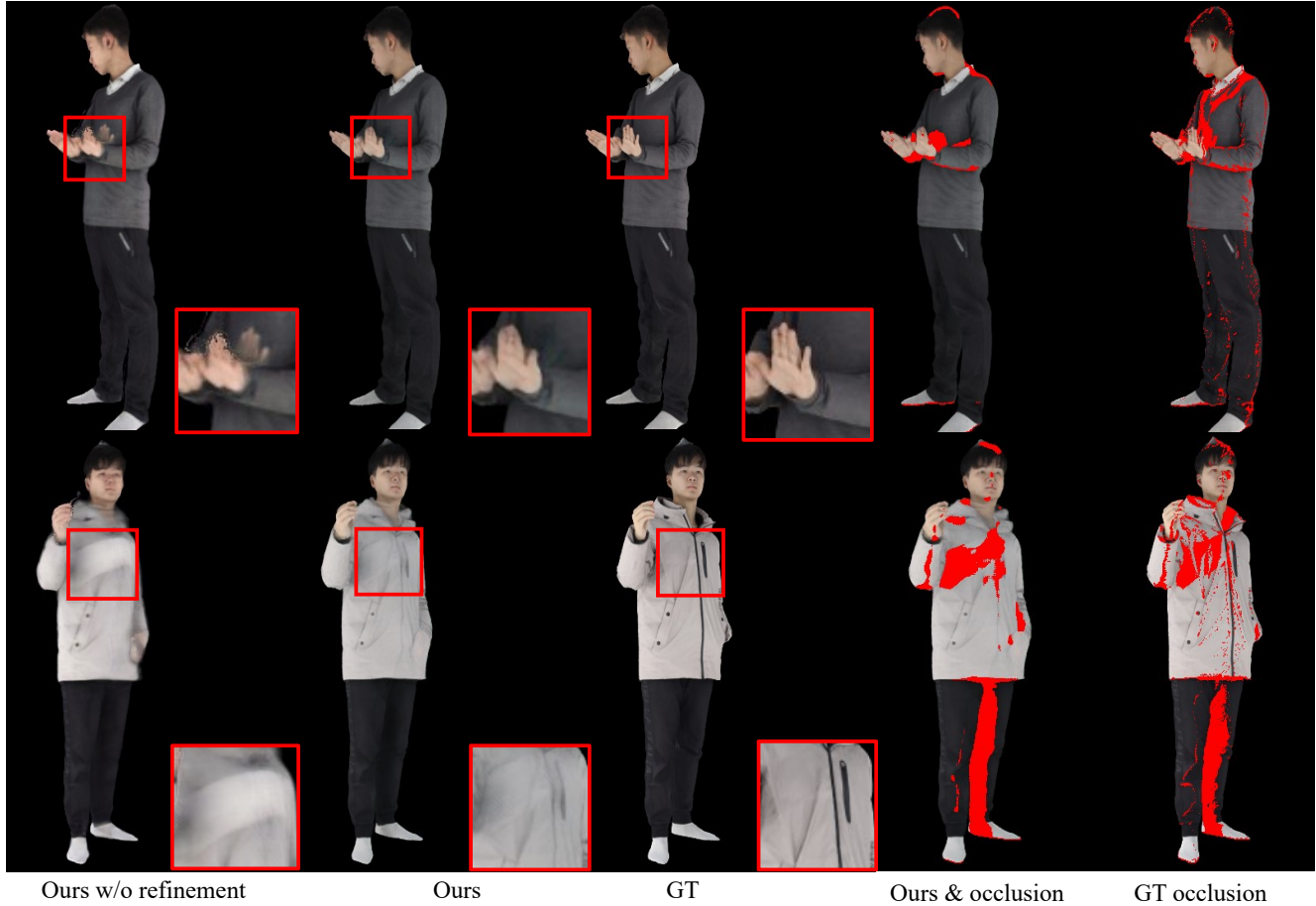


Figure 6. Qualitative results of the ablation studies on handling occluded regions. We use three input views of THuman2.0 dataset to obtain the results. “Ours w/o refinement” denotes the results without using image space refinement. “Ours” denotes the results with image space refinement using occlusion-aware features. “Ours & occlusion” denotes the rendered results with the predicted occlusion mask highlighted in red. “GT occlusion” denotes the ground-truth occlusion mask.

Table 6. Ablation studies of the number of input views on the THuman2.0 dataset. “Interval” denotes the angle between input views.

Views (Interval)	PSNR \uparrow	SSIM \uparrow	LPIPS \downarrow
3 (180°)	31.03	0.970	0.035
4 (90°)	31.73	0.973	0.034
5 (70°)	34.48	0.985	0.023
6 (60°)	34.77	0.986	0.021

4.3.1 Studies on Method Components

We conducted ablation studies to analyze the effectiveness of our method using the THuman2.0 dataset. For the setting without ground-truth depth, we analyzed the effect of using the boundary meshes by removing the sampling guidance of the boundary meshes when sam-

Table 7. Ablation study of fine-tuning the model using images of target subjects on the THuman2.0 dataset. We report the averaged metrics on 125 test subjects for both zero-shot and fine-tuned models.

Samples	PSNR \uparrow	SSIM \uparrow	LPIPS \downarrow
Ours (zero-shot)	31.73	0.973	0.034
Ours (fine-tuned)	36.29	0.988	0.018

pling $\{\mathbf{p}_k\}_{k=1}^K$. Since the boundary meshes are removed, we also removed the usage of the feature \mathbf{g}_{stat} on them. We also analyzed the usage of the SRDF formulation for rendering by replacing the SRDF formulation with the density formulation used in NeRF [30]. Both the quantitative results in Table 3 and the qualitative results in Fig. 5 show that removing the boundary meshes or altering the SRDF formulation degrades the rendering

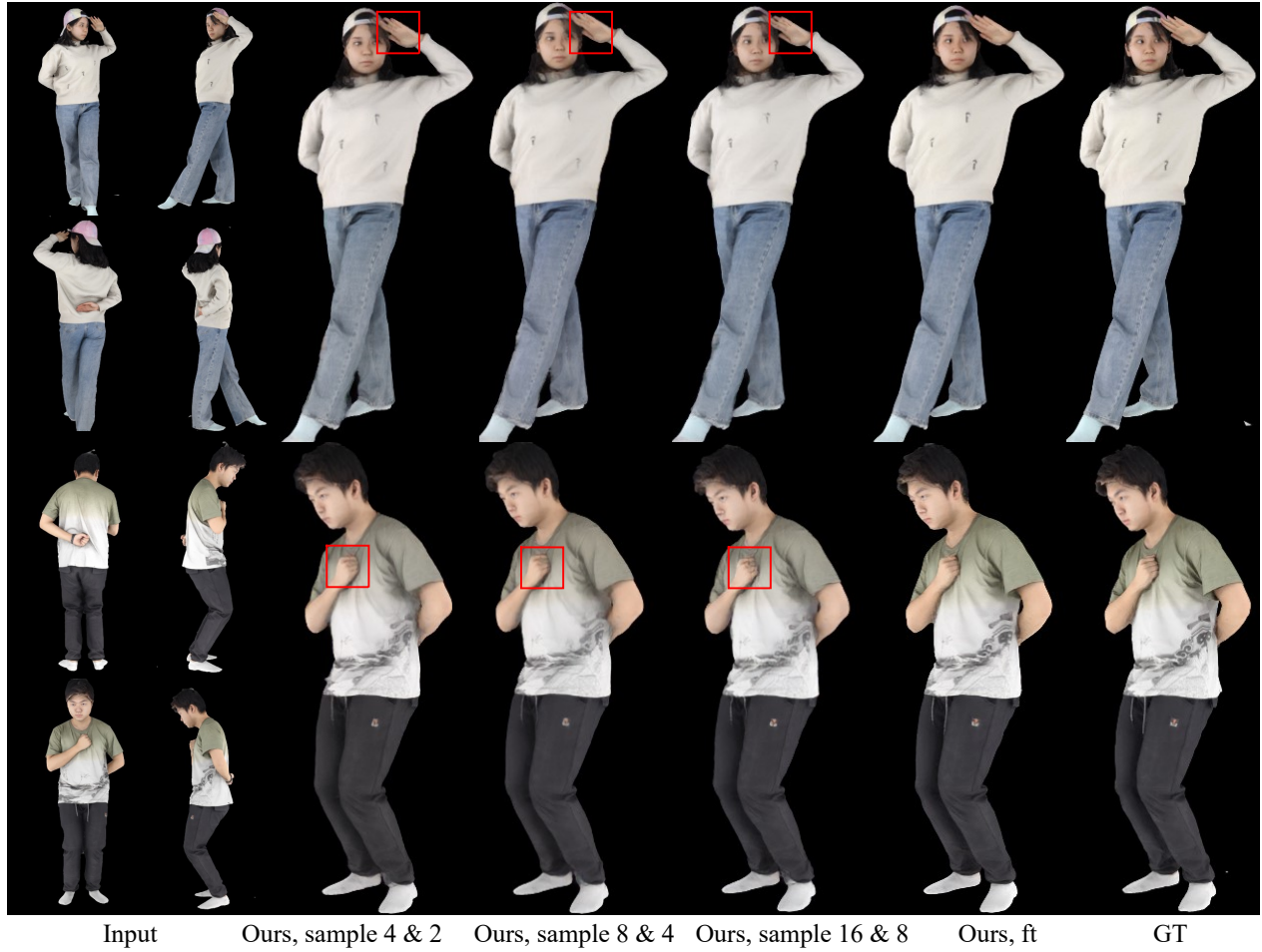


Figure 7. Qualitative results of the ablation studies of the number of samples per ray and the training protocol. “Ours, 4 & 2” denotes our method trained with four samples per ray for sampling guidance and two samples per ray for rendering. “Ours, ft” denotes our method fine-tuned using images of target subjects. While the results from the model using different numbers of samples per ray exhibit similar quality, their rendering of human hands, as shown in the red boxes, are less accurate than the results from the fine-tuned model.

quality.

In the setting using ground-truth depth, we analyzed the effect of the SRDF loss by removing it and only using the depth loss. The results in Table 3 and Fig. 5 show that the SRDF loss further improves the rendering quality.

We also analyzed the effectiveness of our method in handling occluded regions on the THuman2.0 dataset. We used a setting of three input views, which is more likely to contain occluded regions, along with using ground-truth geometry. We compared the results without using the image space refinement with the results using the image space refinement and occlusion-aware features. The results in Table 4 and Fig. 6 show that the image space refinement improves the rendering quality by removing artifacts in occluded regions. We also

visualized the predicted occlusion mask and the ground-truth occlusion mask, demonstrating that occlusion-aware features effectively guide the network to regress the occluded regions.

4.3.2 Studies on Experimental Settings

In addition to ablation studies on the proposed components, we also conducted ablation studies on the number of samples per ray, the number of input views, and the training protocol. The three ablation studies are conducted on the THuman2.0 dataset using four input views and ground-truth geometry. Tables 5 and 6 show the quantitative results of the first two studies, respectively. We observed that our method does not suffer significantly from reducing the number of samples per

ray to a quarter of the original number, namely, $K = 4$ and $L = 2$. The insensitive rendering quality to the number of samples per ray indicates that our method can potentially handle high-resolution images at a similar rendering speed by further reducing the number of samples. Given a view number N_I , we chose the camera poses in the same way described in Sec. 4.1.1, so that a smaller input number results in a larger view interval of $\frac{360^\circ}{N_I}$.

We also conducted an ablation study on the training protocol by fine-tuning the model using images of target subjects. Specifically, we use 32 images of target subjects to fine-tune all trainable parameters of the model. Table 7 shows the averaged quantitative results on 125 test subjects from the THuman2.0 dataset. We observed that fine-tuning the model using images of target subjects further improves the rendering quality. Fig. 7 shows some qualitative results on experimental settings. Please refer to Appendix A for more ablation study results.

5. Conclusion and Future Work

We have presented EG-HumanNeRF, an efficient and generalizable human NeRF method for sparse inputs. Our method outperforms existing quality-prioritized methods in rendering quality and achieves competitive rendering speed compared with speed-prioritized methods. Utilizing the SMPL mesh as a sampling restriction allows our method to render high-quality images with a small number of samples. Without introducing heavyweight generative models, our method improves the rendering quality in occluded regions through occlusion-aware attention and image space refinement. SRDF formulation and the SRDF loss further improve the rendering quality.

5.1. Limitations and Future Work

Our work shares limitations with the optimization-based method utilizing boundary meshes [53]: there may be missing geometries if the boundary meshes does not cover the entire human body, e.g., for humans wearing loose clothes. A possible solution to this issue is to partially loosen the boundary meshes' restriction at the fine-tuning stage.

An interesting direction for future work is to explore the capability of our method handling high-resolution image rendering. To avoid the rendering time increase with the image resolution, we can simply reduce the number of samples per ray, as the output image quality with our method is insensitive to the number of samples per ray. Improving the architecture of the 2D CNN \mathbf{U} for efficient and upsampling to high-resolution images is also a promising direction.

References

- [1] Jonathan T. Barron, Ben Mildenhall, Matthew Tancik, Peter Hedman, Ricardo Martin-Brualla, and Pratul P. Srinivasan. Mip-nerf: A multiscale representation for anti-aliasing neural radiance fields. In *ICCV*, pages 5835–5844, 2021. [2](#)
- [2] Junli Cao, Huan Wang, Pavlo Chemerys, Vladislav Shakhrai, Ju Hu, Yun Fu, Denys Makoviichuk, Sergey Tulyakov, and Jian Ren. Real-time neural light field on mobile devices. In *CVPR*, pages 8328–8337, 2023. [3](#)
- [3] Eric R. Chan, Connor Z. Lin, Matthew A. Chan, Koki Nagano, Boxiao Pan, Shalini De Mello, Orazio Gallo, Leonidas J. Guibas, Jonathan Tremblay, Sameh Khamis, Tero Karras, and Gordon Wetzstein. Efficient geometry-aware 3d generative adversarial networks. In *CVPR*, pages 16102–16112, 2022. [3](#)
- [4] Anpei Chen, Zexiang Xu, Fuqiang Zhao, Xiaoshuai Zhang, Fanbo Xiang, Jingyi Yu, and Hao Su. Mvsnerf: Fast generalizable radiance field reconstruction from multi-view stereo. In *ICCV*, pages 14104–14113, 2021. [3](#)
- [5] Anpei Chen, Zexiang Xu, Andreas Geiger, Jingyi Yu, and Hao Su. Tensorf: Tensorial radiance fields. In *ECCV*, pages 333–350, 2022. [3](#)
- [6] Jianchuan Chen, Ying Zhang, Di Kang, Xuefei Zhe, Linchao Bao, Xu Jia, and Huchuan Lu. Animatable neural radiance fields from monocular rgb videos, 2021. [3](#)
- [7] Jianchuan Chen, Wentao Yi, Liqian Ma, Xu Jia, and Huchuan Lu. Gm-nerf: Learning generalizable model-based neural radiance fields from multi-view images. In *CVPR*, pages 20648–20658, 2023. [2](#), [3](#), [5](#), [6](#), [7](#), [9](#), [10](#), [11](#), [18](#)
- [8] Mingfei Chen, Jianfeng Zhang, Xiangyu Xu, Lijuan Liu, Yujun Cai, Jiashi Feng, and Shuicheng Yan. Geometry-guided progressive nerf for generalizable and efficient neural human rendering. In *ECCV*, pages 222–239, 2022. [2](#), [4](#), [9](#), [11](#)
- [9] Zhiqin Chen, Thomas A. Funkhouser, Peter Hedman, and Andrea Tagliasacchi. Mobilenerf: Exploiting the polygon rasterization pipeline for efficient neural field rendering on mobile architectures. In *CVPR*, pages 16569–16578, 2023. [3](#)
- [10] Wei Cheng, Su Xu, Jingtian Piao, Chen Qian, Wayne Wu, Kwan-Yee Lin, and Hongsheng Li. Generalizable neural performer: Learning robust radiance fields for human novel view synthesis. *CoRR*, abs/2204.11798, 2022. [2](#), [3](#)
- [11] Mingsong Dou, Sameh Khamis, Yury Degtyarev, Philip Davidson, Sean Ryan Fanello, Adarsh Kowdle, Sergio Orts-Escalano, Christoph Rhemann, David Kim, Jonathan Taylor, Pushmeet Kohli, Vladimir Tankovich, and Shahram Izadi. Fusion4d: real-time performance capture of challenging scenes. *ACM Trans. Graph.*, 35(4):114:1–114:13, 2016. [3](#)
- [12] Benjamin Graham, Martin Engelcke, and Laurens van der Maaten. 3d semantic segmentation with sub-

- manifold sparse convolutional networks. In *CVPR*, pages 9224–9232, 2018. 18
- [13] Jiatao Gu, Lingjie Liu, Peng Wang, and Christian Theobalt. Stylererf: A style-based 3d aware generator for high-resolution image synthesis. In *The Tenth International Conference on Learning Representations, ICLR*, pages 1–25, 2022. 3
- [14] Kaiwen Guo, Peter Lincoln, Philip Davidson, Jay Busch, Xueming Yu, Matt Whalen, Geoff Harvey, Sergio Orts-Escalano, Rohit Pandey, Jason Dourgarian, Danhang Tang, Anastasia Tkach, Adarsh Kowdle, Emily Cooper, Mingsong Dou, Sean Ryan Fanello, Graham Fyffe, Christoph Rhemann, Jonathan Taylor, Paul E. Debevec, and Shahram Izadi. The relightables: volumetric performance capture of humans with realistic relighting. *ACM Trans. Graph.*, 38(6):217:1–217:19, 2019. 3
- [15] Peter Hedman, Pratul P. Srinivasan, Ben Mildenhall, Jonathan T. Barron, and Paul Debevec. Baking neural radiance fields for real-time view synthesis. *ICCV*, 2021. 3
- [16] Ke Hong, Zhongming Yu, Guohao Dai, Xinhao Yang, Yaoxiu Lian, Zehao Liu, Ningyi Xu, Yuhang Dong, and Yu Wang. Exploiting hardware utilization and adaptive dataflow for efficient sparse convolution in 3d point clouds. In *Proceedings of the Sixth Conference on Machine Learning and Systems, MLSys*, pages 428–441, 2023. 18
- [17] Tao Hu, Shu Liu, Yilun Chen, Tiancheng Shen, and Jiaya Jia. Efficientnerf - efficient neural radiance fields. In *CVPR*, pages 12892–12901, 2022. 3
- [18] Ajay Jain, Matthew Tancik, and Pieter Abbeel. Putting nerf on a diet: Semantically consistent few-shot view synthesis. In *ICCV 2021*, pages 5865–5874, 2021. 3
- [19] Daiju Kanaoka, Motoharu Sonogashira, Hakaru Tamukoh, and Yasutomo Kawanishi. Manifoldnerf: View-dependent image feature supervision for few-shot neural radiance fields. In *34th British Machine Vision Conference 2023, BMVC 2023*, pages 1–13, 2023.
- [20] Mijeong Kim, Seonguk Seo, and Bohyung Han. Infonerf: Ray entropy minimization for few-shot neural volume rendering. In *CVPR 2022*, pages 12902–12911, 2022. 3
- [21] Andreas Kurz, Thomas Neff, Zhaoyang Lv, Michael Zollhöfer, and Markus Steinberger. Adanerf: Adaptive sampling for real-time rendering of neural radiance fields. In *ECCV*, pages 254–270, 2022. 3
- [22] Youngjoong Kwon, Dahun Kim, Duygu Ceylan, and Henry Fuchs. Neural human performer: Learning generalizable radiance fields for human performance rendering. In *NeurIPS*, pages 24741–24752, 2021. 2, 3
- [23] Youngjoong Kwon, Baole Fang, Yixing Lu, Haoye Dong, Cheng Zhang, Francisco Vicente Carrasco, Albert Mosella-Montoro, Jianjin Xu, Shingo Takagi, Daeil Kim, Aayush Prakash, and Fernando De la Torre. Generalizable human gaussians for sparse view synthesis, 2024. 4
- [24] Yaokun Li, Chao Gou, and Guang Tan. Id-nerf: Indirect diffusion-guided neural radiance fields for generalizable view synthesis, 2024. 2, 3
- [25] Zhe Li, Tao Yu, Zerong Zheng, and Yebin Liu. Robust and accurate 3d self-portraits in seconds. *IEEE Trans. Pattern Anal. Mach. Intell.*, 44(11):7854–7870, 2022. 3
- [26] Haotong Lin, Sida Peng, Zhen Xu, Yunzhi Yan, Qing Shuai, Hujun Bao, and Xiaowei Zhou. Efficient neural radiance fields for interactive free-viewpoint video. In *SIGGRAPH Asia 2022 Conference Papers*, pages 39:1–39:9, 2022. 2, 4, 9, 11
- [27] Lingjie Liu, Jiatao Gu, Kyaw Zaw Lin, Tat-Seng Chua, and Christian Theobalt. Neural sparse voxel fields. In *NeurIPS*, pages 15651–15663, 2020. 3
- [28] Matthew Loper, Naureen Mahmood, Javier Romero, Gerard Pons-Moll, and Michael J. Black. SMPL: a skinned multi-person linear model. *ACM Trans. Graph.*, 34(6):248:1–248:16, 2015. 2, 3
- [29] Marko Mihajlovic, Aayush Bansal, Michael Zollhöfer, Siyu Tang, and Shunsuke Saito. Keypointnerf: Generalizing image-based volumetric avatars using relative spatial encoding of keypoints. In *ECCV*, pages 179–197, 2022. 1, 2, 3, 9, 10, 11
- [30] Ben Mildenhall, Pratul P. Srinivasan, Matthew Tancik, Jonathan T. Barron, Ravi Ramamoorthi, and Ren Ng. Nerf: Representing scenes as neural radiance fields for view synthesis. In *ECCV*, pages 405–421, 2020. 2, 3, 12
- [31] Thomas Müller, Alex Evans, Christoph Schied, and Alexander Keller. Instant neural graphics primitives with a multiresolution hash encoding. *ACM Trans. Graph.*, 41(4):102:1–102:15, 2022. 3
- [32] Thomas Neff, Pascal Stadlbauer, Mathias Panger, Andreas Kurz, Joerg H. Mueller, Chakravarty R. Alla Chaitanya, Anton Kaplanyan, and Markus Steinberger. Donerf: Towards real-time rendering of compact neural radiance fields using depth oracle networks. *Comput. Graph. Forum*, 40(4):45–59, 2021. 3
- [33] Georgios Pavlakos, Vasileios Choutas, Nima Ghorbani, Timo Bolkart, Ahmed A. A. Osman, Dimitrios Tzionas, and Michael J. Black. Expressive body capture: 3D hands, face, and body from a single image. In *CVPR*, pages 10975–10985, 2019. 2, 3
- [34] Sida Peng, Yuanqing Zhang, Yinghao Xu, Qianqian Wang, Qing Shuai, Hujun Bao, and Xiaowei Zhou. Neural body: Implicit neural representations with structured latent codes for novel view synthesis of dynamic humans. In *CVPR*, pages 9054–9063, 2021. 2, 3, 10, 11
- [35] Nikhila Ravi, Jeremy Reizenstein, David Novotny, Taylor Gordon, Wan-Yen Lo, Justin Johnson, and Georgia Gkioxari. Accelerating 3d deep learning with pytorch3d. *arXiv:2007.08501*, 2020. 10
- [36] Christian Reiser, Richard Szeliski, Dor Verbin, Pratul P. Srinivasan, Ben Mildenhall, Andreas Geiger, Jonathan T. Barron, and Peter Hedman. MERF: memory-efficient radiance fields for real-time view synthesis in unbounded scenes. *ACM Trans. Graph.*, 42(4):89:1–89:12, 2023. 3

- [37] Yufan Ren, Tong Zhang, Marc Pollefeys, Sabine Süssstrunk, and Fangjinhua Wang. Volrecon: Volume rendering of signed ray distance functions for generalizable multi-view reconstruction. In *CVPR*, pages 16685–16695, 2023. 3, 7, 8
- [38] Andrew Slavin Ross and Finale Doshi-Velez. Improving the adversarial robustness and interpretability of deep neural networks by regularizing their input gradients. In *Proceedings of the Thirty-Second AAAI Conference on Artificial Intelligence*, pages 1660–1669, 2018. 9
- [39] Ruizhi Shao, Hongwen Zhang, He Zhang, Mingjia Chen, Yanpei Cao, Tao Yu, and Yebin Liu. Doublefield: Bridging the neural surface and radiance fields for high-fidelity human reconstruction and rendering. In *CVPR*, pages 15851–15861, 2022. 3
- [40] Karen Simonyan and Andrew Zisserman. Very deep convolutional networks for large-scale image recognition. In *3rd International Conference on Learning Representations, ICLR 2015, San Diego, CA, USA, May 7-9, 2015, Conference Track Proceedings*, pages 1–14, 2015. 9
- [41] Vincent Sitzmann, Julien N. P. Martel, Alexander W. Bergman, David B. Lindell, and Gordon Wetzstein. Implicit neural representations with periodic activation functions. In *NeurIPS*, pages 7462–7473, 2020. 3
- [42] Shih-Yang Su, Frank Yu, Michael Zollhöfer, and Helge Rhodin. A-nerf: Articulated neural radiance fields for learning human shape, appearance, and pose. In *NeurIPS*, pages 12278–12291, 2021. 3
- [43] Cheng Sun, Min Sun, and Hwann-Tzong Chen. Direct voxel grid optimization: Super-fast convergence for radiance fields reconstruction. In *CVPR*, pages 5449–5459, 2022. 3
- [44] Roman Suvorov, Elizaveta Logacheva, Anton Mashikhin, Anastasia Remizova, Arsenii Ashukha, Aleksei Silvestrov, Naejin Kong, Harshith Goka, Kiwoong Park, and Victor Lempitsky. Resolution-robust large mask inpainting with fourier convolutions. In *WACV*, pages 3172–3182, 2022. 7, 9, 18
- [45] Mingxing Tan and Quoc V. Le. Efficientnetv2: Smaller models and faster training. In *Proceedings of the 38th International Conference on Machine Learning, ICML 2021, 18-24 July 2021, Virtual Event*, pages 10096–10106, 2021. 5, 18
- [46] Daniel Vlasic, Ilya Baran, Wojciech Matusik, and Jovan Popovic. Articulated mesh animation from multi-view silhouettes. *ACM Trans. Graph.*, 27(3):97, 2008. 3
- [47] Daniel Vlasic, Pieter Peers, Ilya Baran, Paul E. Debevec, Jovan Popovic, Szymon Rusinkiewicz, and Wojciech Matusik. Dynamic shape capture using multi-view photometric stereo. *ACM Trans. Graph.*, 28(5):174, 2009. 3
- [48] Ziyu Wan, Christian Richardt, Aljaz Bozic, Chao Li, Vijay Rengarajan, Seonghyeon Nam, Xiaoyu Xiang, Tuotuo Li, Bo Zhu, Rakesh Ranjan, and Jing Liao. Learning neural duplex radiance fields for real-time view synthesis. In *CVPR*, pages 8307–8316, 2023. 3
- [49] Peng Wang, Lingjie Liu, Yuan Liu, Christian Theobalt, Taku Komura, and Wenping Wang. Neus: Learning neural implicit surfaces by volume rendering for multi-view reconstruction. In *NeurIPS*, pages 27171–27183, 2021. 3, 8
- [50] Qianqian Wang, Zhicheng Wang, Kyle Genova, Pratul P. Srinivasan, Howard Zhou, Jonathan T. Barron, Ricardo Martin-Brualla, Noah Snavely, and Thomas A. Funkhouser. Ibrnet: Learning multi-view image-based rendering. In *CVPR*, pages 4690–4699, 2021. 2, 3, 9, 11
- [51] Ting-Chun Wang, Ming-Yu Liu, Jun-Yan Zhu, Andrew Tao, Jan Kautz, and Bryan Catanzaro. High-resolution image synthesis and semantic manipulation with conditional gans. In *CVPR*, pages 8798–8807, 2018. 9
- [52] Zhou Wang, Alan C. Bovik, Hamid R. Sheikh, and Eero P. Simoncelli. Image quality assessment: from error visibility to structural similarity. *IEEE Trans. Image Process.*, 13(4):600–612, 2004. 11
- [53] Zian Wang, Tianchang Shen, Merlin Nimier-David, Nicholas Sharp, Jun Gao, Alexander Keller, Sanja Fidler, Thomas Müller, and Zan Gojcic. Adaptive shells for efficient neural radiance field rendering. *ACM Trans. Graph.*, 42(6), 2023. 3, 14
- [54] Chung-Yi Weng, Brian Curless, Pratul P. Srinivasan, Jonathan T. Barron, and Ira Kemelmacher-Shlizerman. HumanNeRF: Free-viewpoint rendering of moving people from monocular video. In *CVPR*, pages 16210–16220, 2022. 2, 3
- [55] Rundi Wu, Ben Mildenhall, Philipp Henzler, Keunhong Park, Ruiqi Gao, Daniel Watson, Pratul P Srinivasan, Dor Verbin, Jonathan T Barron, Ben Poole, et al. Recomfusion: 3D reconstruction with diffusion priors. In *CVPR*, pages 21551–21561, 2024. 2, 3
- [56] Alex Yu, Rui long Li, Matthew Tancik, Hao Li, Ren Ng, and Angjoo Kanazawa. Plenoctrees for real-time rendering of neural radiance fields. In *ICCV*, pages 5732–5741, 2021. 3
- [57] Alex Yu, Vickie Ye, Matthew Tancik, and Angjoo Kanazawa. pixelnerf: Neural radiance fields from one or few images. In *CVPR*, pages 4578–4587, 2021. 3
- [58] Tao Yu, Jianhui Zhao, Zerong Zheng, Kaiwen Guo, Qionghai Dai, Hao Li, Gerard Pons-Moll, and Yebin Liu. Doublefusion: Real-time capture of human performances with inner body shapes from a single depth sensor. *IEEE Trans. Pattern Anal. Mach. Intell.*, 42(10):2523–2539, 2020. 3
- [59] Tao Yu, Zerong Zheng, Kaiwen Guo, Pengpeng Liu, Qionghai Dai, and Yebin Liu. Function4d: Real-time human volumetric capture from very sparse consumer RGBD sensors. In *CVPR*, pages 5746–5756, 2021. 10, 11
- [60] Kai Zhang, Gernot Riegler, Noah Snavely, and Vladlen Koltun. Nerf++: Analyzing and improving neural radiance fields. *CoRR*, abs/2010.07492, 2020. 2
- [61] Richard Zhang, Phillip Isola, Alexei A. Efros, Eli Shechtman, and Oliver Wang. The unreasonable ef-

- fectiveness of deep features as a perceptual metric. In *CVPR*, pages 586–595, 2018. [11](#)
- [62] Shunyuan Zheng, Boyao Zhou, Ruizhi Shao, Boning Liu, Shengping Zhang, Liqiang Nie, and Yebin Liu. Gps-gaussian: Generalizable pixel-wise 3d gaussian splatting for real-time human novel view synthesis. In *CVPR*, pages 19680–19690, 2024. [1](#), [2](#), [4](#), [8](#), [9](#), [11](#)
- [63] Pierre Zins, Yuanlu Xu, Edmond Boyer, Stefanie Wuhrer, and Tony Tung. Multi-view reconstruction using signed ray distance functions (SRDF). In *CVPR*, pages 16696–16706, 2023. [2](#)

Table 8. Network details of the feature extraction CNN **E** for an input image with size $512 \times 512 \times 3$. Upsample $\times 2$ denotes the bi-linear upsampling operator with a scale factor of 2. “4+5” denotes the sum of the output feature maps with ID 4 and 5.

Operator	Kernel size	Stride	Input ID, Size (HWC)	Output ID, Size (HWC)	#Layers
Conv2D	3	2	0 , $512 \times 512 \times 3$	1 , $256 \times 256 \times 24$	1
Fused_MBConv [45]	3	1	1 , $256 \times 256 \times 24$	2 , $256 \times 256 \times 24$	2
Fused_MBConv [45]	3	2	2 , $256 \times 256 \times 24$	3 , $128 \times 128 \times 48$	4
Upsample $\times 2$	-	-	3 , $128 \times 128 \times 48$	4 , $256 \times 256 \times 48$	1
Conv2D	1	1	2 , $256 \times 256 \times 24$	5 , $256 \times 256 \times 48$	1
Conv2D	3	1	4+5 , $256 \times 256 \times 48$	6 , $256 \times 256 \times 32$	1

Appendix

In this appendix, we provide additional experimental results in Appendix A, and additional implementation details in Appendix B.

A. Additional Experimental Results

We show additional quantitative and qualitative results to provide a comprehensive evaluation. Table 10 shows the quantitative results for each subject fine-tuned with images of target subjects. Fig. 8 shows additional qualitative comparisons with the state-of-the-art methods. Fig. 9 shows additional qualitative results for the ablation study on handling occluded regions.

B. Additional Implementation Details

We first describe implementation details for method components described in Sec. 3.2. We use the first three operators of *EfficientNetV2-S* [45] with an additional residual connection for our feature extraction CNN **E**. Please refer to Table 8 for network details for an input image with size of 512×512 . When sampling using the boundary meshes, the self-intersections on the dilated SMPL-X mesh do not matter since we use either the first or the last intersection point. The self-intersections on the eroded mesh, however, may cause missing geometries, especially for head, hands, and feet. This is because the erosion process causes inward-facing surfaces in complicated body parts. Namely, some geometries are “inside-out”, causing an expansion on part of the eroded mesh and missing geometries. Thus, we remove those body parts from the eroded mesh. Other body parts, i.e., torso, arms and legs have rather simple geometries and do not suffer the problem described above. We implement the 3D CNN **G** following SparseConvNet [12] using *TorchSparse* library [16] for efficient calculation.

For implementation details in Sec. 3.5, the architecture for **U** is based on the 2D neural rendering network described in GM-NeRF [7]. Please refer to Table 9 for details of our CNN **O** that predicts the occlusion map. Finally, the architecture for our discriminator

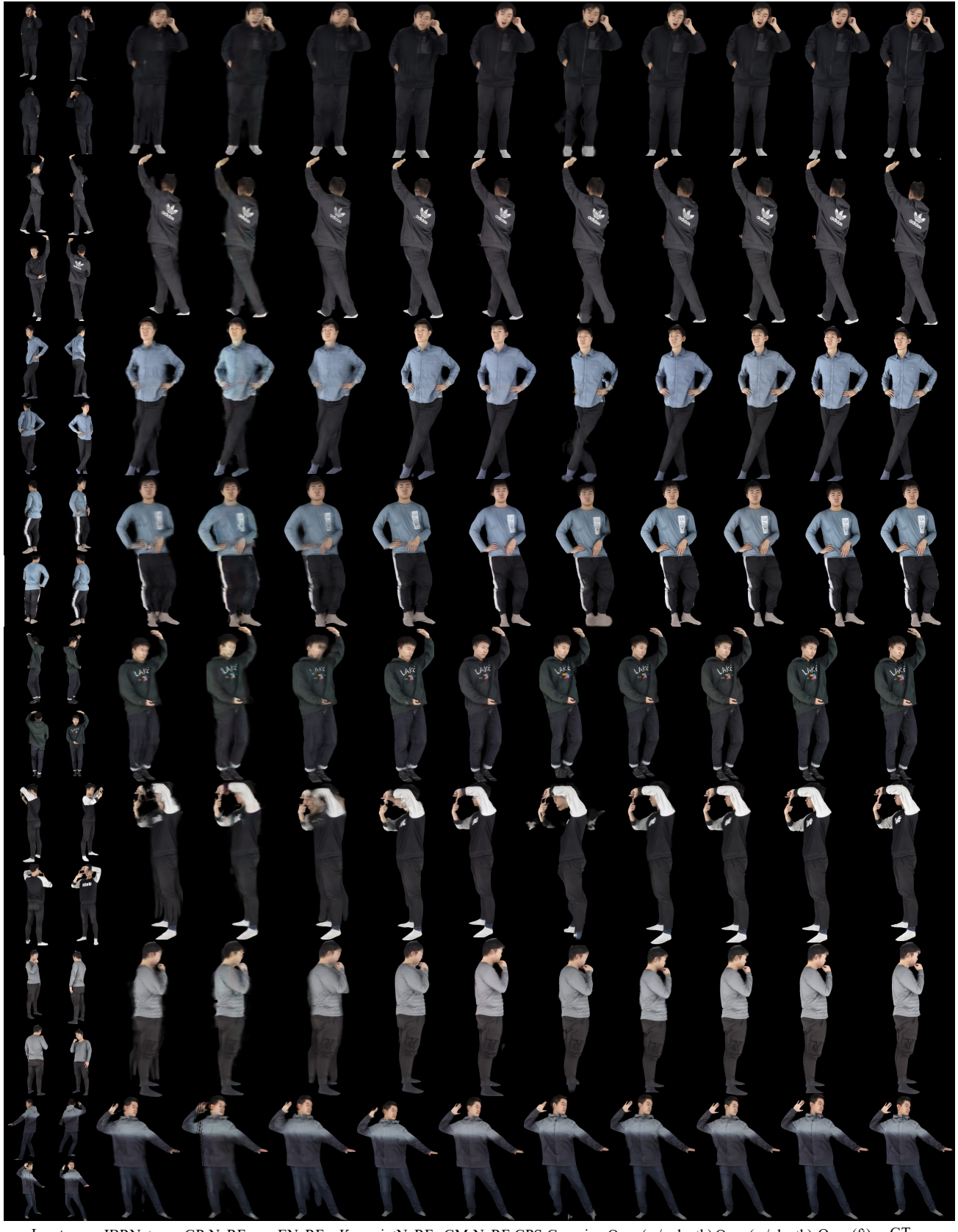
used for adversarial loss is based on the discriminator in LaMa [44].

Table 9. Network details of the feature extraction CNN **O** for an input feature with size $256 \times 256 \times 16$. “ResBlock” denotes the residual block with two convolution-batch-normalization-ReLU layers and a skip connection.

Operator	Kernel size	Stride	Input ID, Size (HWC)	Output ID, Size (HWC)	#Layers
Conv2D	3	1	0 , $256 \times 256 \times 16$	1 , $256 \times 256 \times 96$	1
ResBlock	3	1	1 , $256 \times 256 \times 96$	2 , $256 \times 256 \times 96$	2
TransposedConv	3	2	2 , $256 \times 256 \times 96$	3 , $512 \times 512 \times 96$	1
Conv2D+Sigmoid	1	1	3 , $512 \times 512 \times 96$	4 , $512 \times 512 \times 1$	1

Table 10. Quantitative results for each subject fine-tuned with images of target subjects on the THuman2.0 dataset.

Subject	PSNR	SSIM	LPIPS												
401	31.95	0.989	0.018	402	34.06	0.989	0.023	403	23.69	0.933	0.073	404	39.03	0.991	0.015
405	41.01	0.994	0.013	406	34.99	0.993	0.016	407	33.93	0.990	0.017	408	34.08	0.979	0.036
409	39.37	0.995	0.012	410	37.46	0.993	0.015	411	34.83	0.988	0.020	412	38.14	0.995	0.011
413	35.96	0.993	0.016	414	35.11	0.992	0.016	415	36.57	0.992	0.016	416	37.97	0.991	0.015
417	35.46	0.992	0.015	418	35.43	0.992	0.017	419	38.18	0.993	0.016	420	38.35	0.993	0.015
421	37.01	0.993	0.016	422	41.91	0.994	0.014	423	39.16	0.994	0.013	424	39.44	0.994	0.012
425	38.00	0.993	0.014	426	38.65	0.991	0.015	427	39.38	0.995	0.013	428	37.81	0.993	0.017
429	37.80	0.994	0.013	430	38.06	0.992	0.015	431	39.31	0.994	0.013	432	38.19	0.995	0.011
433	38.11	0.995	0.011	434	37.84	0.991	0.015	435	38.14	0.985	0.028	436	33.34	0.960	0.054
437	39.04	0.992	0.016	438	35.75	0.990	0.020	439	39.31	0.995	0.014	440	35.65	0.994	0.016
441	38.44	0.994	0.015	442	37.04	0.989	0.020	443	32.36	0.984	0.024	444	32.92	0.988	0.021
445	37.72	0.990	0.018	446	41.52	0.996	0.010	447	38.55	0.993	0.017	448	39.63	0.996	0.013
449	40.87	0.994	0.013	450	37.53	0.994	0.013	451	34.97	0.993	0.012	452	36.64	0.993	0.013
453	35.10	0.992	0.014	454	35.82	0.994	0.012	455	33.22	0.988	0.018	456	33.51	0.989	0.018
457	36.45	0.993	0.014	458	37.40	0.994	0.014	459	36.46	0.993	0.016	460	35.17	0.992	0.017
461	35.26	0.992	0.014	462	34.88	0.991	0.014	463	35.01	0.989	0.018	464	40.25	0.993	0.015
465	39.37	0.988	0.024	466	38.59	0.991	0.016	467	36.11	0.986	0.026	468	38.46	0.995	0.011
469	37.13	0.994	0.013	470	35.93	0.994	0.014	471	39.59	0.995	0.011	472	38.95	0.994	0.013
473	38.80	0.994	0.013	474	38.83	0.992	0.014	475	38.70	0.992	0.016	476	38.03	0.993	0.013
477	36.41	0.992	0.014	478	41.85	0.995	0.010	479	40.41	0.995	0.014	480	40.13	0.994	0.013
481	31.96	0.979	0.036	482	35.86	0.992	0.015	483	38.65	0.994	0.013	484	30.40	0.977	0.033
485	35.59	0.992	0.016	486	36.44	0.992	0.015	487	36.86	0.993	0.017	488	31.89	0.980	0.030
489	37.42	0.995	0.011	490	34.79	0.989	0.016	491	36.98	0.993	0.015	492	36.96	0.994	0.012
493	35.97	0.991	0.018	494	28.08	0.973	0.037	495	35.49	0.994	0.013	496	34.55	0.991	0.015
497	32.79	0.983	0.029	498	36.59	0.993	0.013	499	38.21	0.992	0.016	500	37.76	0.992	0.015
501	37.51	0.991	0.017	502	38.18	0.995	0.013	503	38.60	0.994	0.015	504	39.48	0.994	0.014
505	39.42	0.995	0.009	506	40.75	0.993	0.015	507	34.35	0.987	0.018	508	24.98	0.818	0.085
509	23.47	0.788	0.075	510	38.88	0.995	0.011	511	35.99	0.987	0.029	512	31.52	0.982	0.023
513	37.14	0.990	0.017	514	35.53	0.993	0.015	515	33.92	0.988	0.021	516	33.91	0.990	0.020
517	30.89	0.981	0.031	518	32.43	0.986	0.023	519	33.54	0.992	0.012	520	33.05	0.990	0.013
521	34.30	0.992	0.011	522	32.53	0.988	0.021	523	33.38	0.989	0.019	524	34.46	0.993	0.013
525	33.52	0.990	0.018	Average	36.29	0.988	0.018								



Input IBRNet GP-NeRF ENeRF KeypointNeRF GM-NeRF GPS-Gaussian Ours (w/o depth) Ours (w/ depth) Ours (ft) GT

Figure 8. Additional qualitative evaluation results on the THuman2.0 dataset compared with the state-of-the-art methods. The experimental settings are the same as in Fig. 4.



Figure 9. Additional ablation study results on handling occluded regions. The experimental settings are the same as in Fig. 6.